

Magneto-optical properties of multilayer graphenes

Mikito Koshino and Tsuneya Ando

*Department of Physics, Tokyo Institute of Technology
2-12-1 Ookayama, Meguro-ku, Tokyo 152-8551, Japan*

(Dated: October 22, 2018)

The magneto-optical absorption properties of graphene multilayers are theoretically studied. It is shown that the spectrum can be decomposed into sub-components effectively identical to the monolayer or bilayer graphene, allowing us to understand the spectrum systematically as a function of the layer number. Odd-layered graphenes always exhibit absorption peaks which shifts in proportion to \sqrt{B} , with B being the magnetic field, due to the existence of an effective monolayer-like subband. We propose a possibility of observing the monolayer-like spectrum even in a mixture of multilayer graphene films with various layers numbers.

I. INTRODUCTION

The unusual electronic property of the atomically thin graphene films has been of great interest. Recently the optical absorption spectra were measured in graphene-related systems under magnetic fields.^{1,2,3,4,5,6} In this paper we theoretically study magneto-optical spectra of the graphene multilayer.

The monolayer graphene is a zero-gap semiconductor with the linear dispersion analogous to the zero-mass relativistic particle. In presence of a magnetic field B , it gives an unusual sequence of the Landau levels with spacing proportional to \sqrt{B} in both of the electron and hole sides.⁷ The transport properties in such a unique band structure were studied and found to be significantly different from the conventional system.^{8,9,10,11,12,13} Recent experimental realizations of monocrystalline graphene opened the way for direct probing of those unusual properties.^{14,15,16} The Landau level structure of the single-atomic sheet of graphene was investigated through the quantum Hall effect^{15,16} and the cyclotron resonance.^{2,3} The optical response in graphene monolayer was theoretically studied.^{11,17,18}

The multilayer systems containing few layers of graphene are also fabricated,^{15,19} have attracted broad interest as well.²⁰ There the interlayer coupling drastically changes the structure around the band touching point.^{19,21,22,23,24,25,26,27,28} On the other hand, recent observations of the magneto-absorption spectra of thin epitaxial graphite¹ show \sqrt{B} -dependent transition peaks just as in monolayer graphene.^{2,3} Similar evidences for the linear dispersion were also found in thicker graphite systems.^{4,5,29,30} Quite recently the cyclotron resonance was measured in graphene bilayer.⁶ In theories, the electronic structure in magnetic fields has been extensively studied for three-dimensional (3D) graphite^{7,31,32,33,34,35} and for few-layers graphenes.^{21,24,37} The optical absorption was theoretically investigated for the bilayer graphene.^{36,37}

Here we study the optical absorption properties of the AB-stacked multilayer graphenes in magnetic fields systematically as a function of the layer number. We decompose the Hamiltonian into subsystems effectively iden-

tical to monolayer or bilayer graphene,²⁸ and express the spectrum as a summation over each of them. We present in Sec. II the Hamiltonian decomposition and the Landau-level structure of the multilayer graphene as well as the formulation of the optical absorption. We show the numerical results in Sec. III and discussion in Sec. IV.

II. FORMULATION

We consider a multilayer graphene composed of N layers of a carbon hexagonal network, which are arranged in the AB (Bernal) stacking. The system can be described by a $\mathbf{k}\cdot\mathbf{p}$ Hamiltonian based on 3D graphite model.^{39,40,41} The effective models were derived for the monolayer graphene,^{7,42,43,44} the bilayer,²¹ and the trilayer and more.^{24,28} For the simplicity we include the nearest-neighbor intra-layer coupling parameter γ_0 , and the inter-layer coupling γ_1 between A and B atoms located vertically with respect to the layer plane. The band parameters were experimentally estimated in bulk graphite as $\gamma_0 \approx 3.16$ eV²⁹ and $\gamma_1 \approx 0.39$ eV.⁴⁵ The effects of other band parameters neglected here will be discussed in Sec. IV.

The low energy spectrum is given by the states in the vicinity of K and K' points in the Brillouin zone. Let $|A_j\rangle$ and $|B_j\rangle$ be the Bloch functions at the K point, corresponding to the A and B sublattices, respectively, of layer j . For convenience we divide carbon atoms into two groups as

$$\text{Group I : } B_1, A_2, B_3, \dots \quad (1)$$

$$\text{Group II : } A_1, B_2, A_3, \dots \quad (2)$$

The atoms of group I are arranged along vertical columns normal to the layer plane, while those in group II are above or below the center of hexagons in the neighboring layers. The lattice constant within a layer is given by $a = 0.246$ nm and the distance between adjacent layers $c_0/2 = 0.334$ nm.

If the basis is taken as $|A_1\rangle, |B_1\rangle; |A_2\rangle, |B_2\rangle; \dots; |A_N\rangle, |B_N\rangle$, the Hamiltonian for the multilayer graphene

around the K point becomes

$$\mathcal{H} = \begin{pmatrix} H_0 & V & & & \\ V^\dagger & H_0 & V^\dagger & & \\ & V & H_0 & V & \\ & & & \ddots & \ddots & \ddots \end{pmatrix}, \quad (3)$$

with

$$H_0 = \begin{pmatrix} 0 & v\pi_- \\ v\pi_+ & 0 \end{pmatrix}, \quad V = \begin{pmatrix} 0 & 0 \\ \gamma_1 & 0 \end{pmatrix}. \quad (4)$$

where $\pi_\pm = \pi_x \pm i\pi_y$ with $\boldsymbol{\pi} = -i\hbar\nabla + e\mathbf{A}$, the vector potential \mathbf{A} , and v is the band velocity of monolayer graphene, which is related to the band parameter via $v = \sqrt{3}a\gamma_0/2\hbar$. The effective Hamiltonian for K' is obtained by exchanging π_+ and π_- .

The Hamiltonian (3) can be decomposed into smaller subsystems for the basis appropriately chosen.²⁸ First, we define the orthonormal sets

$$\begin{aligned} |\phi_l^{(\text{I})}\rangle &= \psi_l(1)|B_1\rangle + \psi_l(2)|A_2\rangle + \psi_l(3)|B_3\rangle + \dots, \\ |\phi_l^{(\text{II})}\rangle &= \psi_l(1)|A_1\rangle + \psi_l(2)|B_2\rangle + \psi_l(3)|A_3\rangle + \dots, \end{aligned} \quad (5)$$

where

$$\psi_l(j) = \sqrt{\frac{2}{N+1}} \sin j\kappa_l, \quad \kappa_l = \frac{\pi}{2} - \frac{l\pi}{2(N+1)}, \quad (6)$$

with

$$l = -(N-1), -(N-3), \dots, N-1. \quad (7)$$

Here, l is an odd integer when the layer number N is even, while l is even when N is odd, and therefore $l=0$ is allowed only for odd N .

Next, for $m > 0$, we take the basis

$$\left\{ (|\phi_m^{(\text{I})}\rangle + |\phi_{-m}^{(\text{II})}\rangle)/\sqrt{2}, (|\phi_m^{(\text{II})}\rangle + |\phi_{-m}^{(\text{I})}\rangle)/\sqrt{2}, \right. \\ \left. (|\phi_m^{(\text{I})}\rangle - |\phi_{-m}^{(\text{II})}\rangle)/\sqrt{2}, (|\phi_m^{(\text{II})}\rangle - |\phi_{-m}^{(\text{I})}\rangle)/\sqrt{2} \right\}. \quad (8)$$

For $m = 0$, we take the basis $\{|\phi_0^{(\text{I})}\rangle, |\phi_0^{(\text{II})}\rangle\}$. Then, the Hamiltonian has no off-diagonal elements between different m 's. For $m > 0$, the sub-Hamiltonian within the basis Eq. (8) becomes

$$\mathcal{H}_m = \begin{pmatrix} 0 & v\pi_- & 0 & 0 \\ v\pi_+ & 0 & \lambda_m\gamma_1 & 0 \\ 0 & \lambda_m\gamma_1 & 0 & v\pi_- \\ 0 & 0 & v\pi_+ & 0 \end{pmatrix}, \quad (9)$$

with

$$\lambda_m = 2 \cos \kappa_m, \quad (10)$$

which is equivalent to the Hamiltonian of bilayer graphene, while the inter-layer coupling γ_1 is multiplied by λ_m . For $m = 0$, we have

$$\mathcal{H}_{m=0} = \begin{pmatrix} 0 & v\pi_- \\ v\pi_+ & 0 \end{pmatrix}, \quad (11)$$

which is identical to the Hamiltonian of the monolayer graphene. These subsystems are labeled as

$$\begin{aligned} m &= 0, 2, 4, \dots, N-1 \quad (\text{odd } N), \\ m &= 1, 3, 5, \dots, N-1 \quad (\text{even } N). \end{aligned} \quad (12)$$

The eigenstate of a finite-layered graphene can be regarded as a part of a standing wave in 3D limit, which is a superposition of opposite traveling waves with $\pm k_z$. The quantity κ ($= \kappa_m$) in our representation corresponds to the 3D wave number via $\kappa = |k_z|c_0/2$. Thus the monolayer-type subband $\kappa = \pi/2$ is related to a H point in the 3D Brillouin zone, while no states exactly correspond to $k_z = 0$ since κ never becomes zero.

The Landau levels of the monolayer-type states are given by

$$\varepsilon_{sn} = s\Delta_B\sqrt{n}, \quad (13)$$

with $n = 0, 1, \dots$ and $s = \pm$, where $s = +$ and $-$ represent the electron and hole bands, respectively, and only $s = +$ is allowed for $n = 0$.⁷ Here Δ_B is the magnetic energy, defined by

$$\Delta_B = \sqrt{2\hbar v^2 eB}. \quad (14)$$

The Landau-level structure of the bilayer-type Hamiltonian (9) was obtained previously⁴⁶ and can be analytically derived by noting that π_\pm are associated with the ascending / descending operators of the Landau levels²⁴ in a similar way to that for 3D graphite.^{31,32} The eigenfunction can be written as

$$(c_1\varphi_{n-1,k}, c_2\varphi_{n,k}, c_3\varphi_{n,k}, c_4\varphi_{n+1,k}), \quad (15)$$

with $n \geq -1$ and amplitudes c_i . Here $\varphi_{n,k}(x, y)$ is the wavefunction of the n th Landau level in conventional two-dimensional system, given in the Landau gauge $\mathbf{A} = (0, Bx)$ by $\varphi_{n,k} = i^n (2^n n! \sqrt{\pi} l)^{-1/2} e^{iky} e^{-z^2/2} H_n(z)$ with $z = (x + kl^2)/l$ and H_n being the Hermite polynomial. We define $\varphi_{n,k} \equiv 0$ for $n < 0$.

For $n \geq 1$, the Hamiltonian matrix for the vector (c_1, c_2, c_3, c_4) then becomes

$$\begin{pmatrix} 0 & \Delta_B\sqrt{n} & 0 & 0 \\ \Delta_B\sqrt{n} & 0 & \lambda\gamma_1 & 0 \\ 0 & \lambda\gamma_1 & 0 & \Delta_B\sqrt{n+1} \\ 0 & 0 & \Delta_B\sqrt{n+1} & 0 \end{pmatrix}, \quad (16)$$

where the index of λ_m is dropped. This immediately gives four eigen values

$$\varepsilon_{n,\mu,s} = \frac{s}{\sqrt{2}} \left[(\lambda\gamma_1)^2 + (2n+1)\Delta_B^2 \right. \\ \left. + \mu \sqrt{(\lambda\gamma_1)^4 + 2(2n+1)(\lambda\gamma_1)^2\Delta_B^2 + \Delta_B^4} \right]^{1/2}, \quad (17)$$

where $\mu = \pm$ correspond to the higher and lower subbands in the limit of zero magnetic field, respectively.²¹

In the following we use the notation $\mu = H, L$ instead of $+, -$ to avoid the confusion with $s = \pm$. The eigen states can be labeled by n, μ, s , and k .

For $n = 0$, the first component of the wave function (15) disappears and we have only three levels,

$$\varepsilon_{0,L} = 0, \quad (18)$$

$$\varepsilon_{0,H,s} = s\sqrt{\gamma_1^2 + \Delta_B^2}. \quad (19)$$

At $n = -1$ only the last component survives in (15) so that we have only a single level in the lower subband, $\varepsilon_{-1,L} = 0$ (the level $\varepsilon_{-1,H}$ does not exist).

In small magnetic fields, the Landau levels for the lower subband in the region $\varepsilon \ll \lambda\gamma_1$ are approximately given by $\varepsilon_{n,L,s} \approx s(\hbar eB/m^*)\sqrt{n(n+1)}$ with the effective mass $m^* = \lambda\gamma_1/(2v^2)$.²¹ Thus the level spacing shrinks much faster in $B \rightarrow 0$ than that in the monolayer $\propto \sqrt{B}$. The ratio of the first gap of the bilayer-type subband, $\hbar eB/m^*$, to that of the monolayer, Δ_B , is given by $\Delta_B/(\lambda\gamma_1)$.

Figure 1 shows the Landau levels of the bilayer-type Hamiltonian as a function of κ , in the magnetic field given by $\Delta_B/\gamma_1 = 0.5$. The bilayer levels become those of two independent monolayers at $\kappa = \pi/2$, where the effective inter-layer coupling $\lambda\gamma_1$ vanishes. The levels become flat around $\kappa = 0$, where $d\lambda/d\kappa$ vanishes. In the bottom panel we show the list of κ for every layer number N . The top and bottom panels share the horizontal axis; the Landau levels in the specific point in the bottom panel are shown directly above.

The velocity operator for the sub-Hamiltonian \mathcal{H}_m is given by $v_x = -(i/\hbar)[x, \mathcal{H}_m] = \partial\mathcal{H}_m/\partial\pi_x$. There are no matrix elements connecting different m 's. For bilayer-type subband, v_x has a non-zero matrix element only between the Landau levels with n and $n \pm 1$ for arbitrary combinations of $\mu = H, L$ and $s = \pm$. This is explicitly written as

$$\langle n', \mu', s'; k' | v_x | n, \mu, s; k \rangle = v\delta_{k,k'} [(c_1'^* c_2 + c_3'^* c_4)\delta_{n,n'-1} + (c_2'^* c_1 + c_4'^* c_3)\delta_{n,n'+1}], \quad (20)$$

where c_i and c_i' are the eigenvectors of the matrix (16), corresponding to the Landau levels (n, μ, s) and (n', μ', s') , respectively. For the monolayer-type band, we have

$$\langle n', s'; k' | v_x | n, s; k \rangle = v\delta_{k,k'} [c_1'^* c_2 \delta_{n,n'-1} + c_2'^* c_1 \delta_{n,n'+1}], \quad (21)$$

where (c_1, c_2) is $(0, 1)$ for $n = 0$ and $(s, 1)/\sqrt{2}$ for $n \geq 1$ for K -point.⁸

To estimate the optical absorption intensity, we calculate the real part of the dynamical conductivity $\sigma_{xx}(\omega)$. The relative transmission of the sheet to the vacuum, for the linearly polarized light incident perpendicular to the plane, is related to this quantity via³⁸

$$T = \left| 1 + \frac{2\pi}{c} \sigma_{xx}(\omega) \right|^{-2} \approx 1 - \frac{4\pi}{c} \text{Re} \sigma_{xx}(\omega). \quad (22)$$

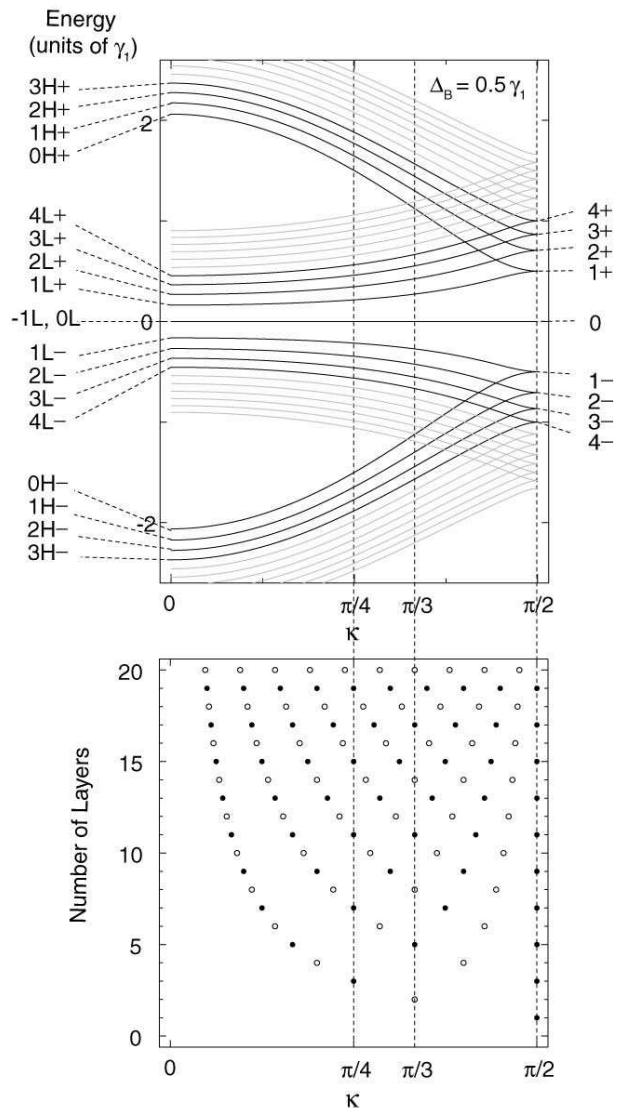


FIG. 1: (top) Landau levels of the bilayer-type subband as a function of κ with $\lambda = 2 \cos \kappa$. Magnetic field strength is taken as $\Delta_B/\gamma_1 = 0.5$. (bottom) Lists of κ in N -layered graphene. Empty and filled circles represent even and odd N 's, respectively.

As will be shown below, the expansion is valid except in thick multilayer graphenes for which the absorption is significant. The dynamical conductivity can be written in usual manner as

$$\sigma_{xx}(\omega) = \frac{e^2 \hbar}{iS} \sum_{\alpha, \beta} \frac{f(\varepsilon_\alpha) - f(\varepsilon_\beta)}{\varepsilon_\alpha - \varepsilon_\beta} \frac{|\langle \alpha | v_x | \beta \rangle|^2}{\varepsilon_\alpha - \varepsilon_\beta + \hbar\omega + i\delta}, \quad (23)$$

where S is the area of the system, v_x is the velocity operator, δ is the positive infinitesimal, $f(\varepsilon)$ is the Fermi distribution function, and $|\alpha\rangle$ and ε_α describe the eigenstate and the eigen energy of the system.

In the simplest approximation, we include the disorder effect by replacing δ with the phenomenological constant

$\hbar/\tau \equiv 2\Gamma$ and taking the ideal eigenstates as α, β . The conductivity can then be written as a summation over all the contributions of the subsystems, which are independently calculated. Correspondingly, we compute the density of states per unit area as

$$D(\varepsilon) = -\frac{1}{\pi S} \text{Im} \sum_{\alpha} \frac{1}{\varepsilon - \varepsilon_{\alpha} + i\Gamma}, \quad (24)$$

with the ideal eigenstates α .

The dynamical conductivity at zero magnetic field was calculated for the monolayer^{11,17} and the bilayer graphene.³⁶ For the ideal monolayer at $\varepsilon_F = 0$, the expression apart from $\omega = 0$ becomes a frequency-independent value^{11,17}

$$\text{Re} \sigma_{xx}(\omega) = \frac{g_v g_s}{16} \frac{e^2}{\hbar}, \quad (25)$$

with $g_v = 2$ being the valley (K, K') degeneracy and $g_s = 2$ the spin degeneracy. Note that the dynamical conductivity has a singularity at $(\varepsilon_F, \omega) = (0, 0)$, which is removed if level-broadening effect is included properly.¹¹ The expression for the effective bilayer Hamiltonian (9) with $\varepsilon_F = 0$ is given by³⁶

$$\text{Re} \sigma_{xx}(\omega) = \frac{g_v g_s}{16} \frac{e^2}{\hbar} \left[\frac{2\lambda^2 \gamma_1^2}{\hbar^2 \omega^2} \theta(\hbar\omega - \lambda\gamma_1) + \frac{\hbar\omega - 2\lambda\gamma_1}{\hbar\omega - \lambda\gamma_1} \theta(\hbar\omega - 2\lambda\gamma_1) + \frac{\hbar\omega + 2\lambda\gamma_1}{\hbar\omega + \lambda\gamma_1} \right], \quad (26)$$

where $\theta(x) = 1$ for $x > 0$ and $\theta(x) = 0$ for $x < 0$. The above shows that the typical value of the real part of the conductivity for $\hbar\omega/\gamma_1 < 1$ is $(g_v g_s/16)(e^2/\hbar)$ per layer. By noting that $e^2/\hbar c \approx 1/137$, we see that the expansion in Eq. (22) is valid roughly for $N \lesssim 20$.

III. NUMERICAL RESULTS

Figure 2 shows the plots of $\text{Re} \sigma_{xx}(\omega)$ for the monolayer and bilayer graphenes in several magnetic fields. Here we take $\Gamma/\gamma_1 = 0.01$, $\varepsilon_F = 0$, and zero temperature. Dotted lines penetrating panels represent the transition energies between several specific Landau levels as a continuous function of Δ_B . The peak positions of each panel correspond to the intersections of those and the bottom line of the panel.

In the monolayer the peak position obviously shifts in proportion to \sqrt{B} (i.e., $\propto \Delta_B$). In the limit of vanishing magnetic field, the conductivity eventually becomes the value given by Eq. (25). The spectrum in the bilayer is rather complicated; starting from $\omega = 0$, we first see the series of the transition peaks within L bands from $\omega = 0$, and then those between L and H enter for $\hbar\omega \gtrsim \gamma_1$ and lastly those within H bands for $\hbar\omega \gtrsim 2\gamma_1$. The every peak position behaves as a linear function of B ($\propto \Delta_B^2$) in weak fields but it switches over to \sqrt{B} -dependence as the corresponding energy is going out of the parabolic

band region. In small fields the peaks are smeared out more easily in the bilayer than in the monolayer. The conductivity converges to the zero-field curve with a step-like structure at $\varepsilon = \gamma_1$, which is expressed as Eq. (26) in the clean limit.

Figure 3 shows the plots of $\text{Re} \sigma_{xx}(\omega)$ from $N = 1$ to 5 with two different magnetic fields with $\Delta_B/\gamma_1 = 0.1$ and 0.2. We again take $\Gamma/\gamma_1 = 0.01$, $\varepsilon_F = 0$, and zero temperature. The results are shown separately for each subband. In every odd layers the monolayer-type subband gives the identical spectrum. All other bilayer-types give different spectra depending on λ . The quantized feature is more easily resolved in a subband with a smaller λ , because of its narrower level spacings. In zero field limit, every bilayer-type spectrum has a step at $\varepsilon \sim \lambda\gamma_1$, where the excitation between L and H bands starts.

It is intriguing to consider how the absorption spectrum looks like when the sample is a mixture of thin graphene films with various layer numbers. One might think the discreteness of κ is easily smeared out and we just get the 3D limit, but it is not always the case as we will show in the following. We here calculate the dynamical conductivity averaged over the samples $N = 1, 2, 3, \dots, 20$. We show in Fig. 4 plots of $\text{Re} \sigma_{xx}(\omega)$ for different magnetic fields with $\Delta_B/\gamma_1 = 0.1, 0.2$, and 0.3 and in Fig. 5 a gray-scale plot of $\text{Re} \sigma_{xx}(\omega, \Delta_B)$.

Surprisingly we still see the series of peaks in the monolayer graphene $\hbar\omega \propto \sqrt{B}$. This comes from the monolayer-type subbands which appears in every odd layered graphene. The visibility of the monolayer-type signal depends on the ratio of the number of monolayer-type subbands to the total; in the present case, this is 10 to 110. We expect that the signal of monolayer gradually becomes invisible as the maximum layer number N_{max} becomes larger, because the total subband number increases as $\propto N_{\text{max}}^2$ while the number of monolayer-type as $\propto N_{\text{max}}$.

We have another set of dominant peaks, which can be identified as the bilayer-type with $\kappa = 0$ ($\lambda = 2$). Although there is no subband which exactly takes this value, many subbands around $\kappa \sim 0$ have almost the same peak positions as the Landau level is flat against κ there and gives similar spectra. Every peak shifts upward with respect to the original position of $\kappa = 0$, since the Landau level spacing is generally wider for larger κ . Unlike the monolayer-type signal, this would survive even in the 3D limit, since the finite region in κ (not a point) can contribute to this spectrum. When decreasing the magnetic field, however, the bilayer-type peaks are immediately blurred due to rapid B -linear dependence, while the monolayer peaks survive even in relatively smaller magnetic field. In zero-field limit, we are left with a bump at $\hbar\omega = 2\gamma_1$, which comes from the H - L transition step of the bilayer-type subbands with $\kappa \sim 0$.

Just in the same way as the monolayer-type subband ($\kappa = \pi/2$) appears in every two layers, the bilayer-type subband with $\kappa = \pi/3$ enters in every three layers ($N = 2, 5, 8, \dots$) and that with $\kappa = \pi/4$ in every four layers

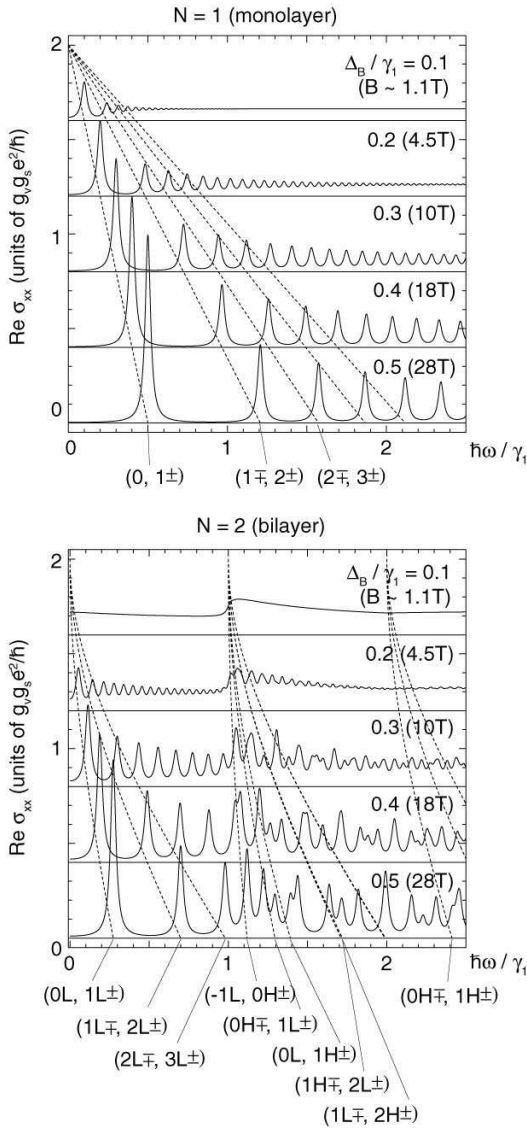


FIG. 2: Real part of the dynamical conductivity of the monolayer (top) and bilayer (bottom) graphenes plotted against the frequency ω , calculated for different magnetic fields (specified by Δ_B) and $\Gamma/\gamma_1 = 0.01$. Dashed curves indicate the transition energies between several Landau levels in the ideal limit.

($N = 3, 7, 11, \dots$). We can see the H - L transition peaks of those κ 's in Fig. 5, while L - L peaks are hidden by other dominant contributions.

The similar analysis is available for the density of states (DOS). In Fig. 6, the top panel shows DOS averaged over $N = 1, 2, 3, \dots, 20$ as a function of the Fermi energy. The bottom panel shows the corresponding plot for the local density of states (LDOS) on the *top layer*, defined by the number of states per unit energy width and per unit area on the layer. We also present in Fig. 7 the two-dimensional plots of DOS and LDOS on (ϵ, Δ_B) -plane, where the gray-scale shows the relative value from the zero magnetic field.

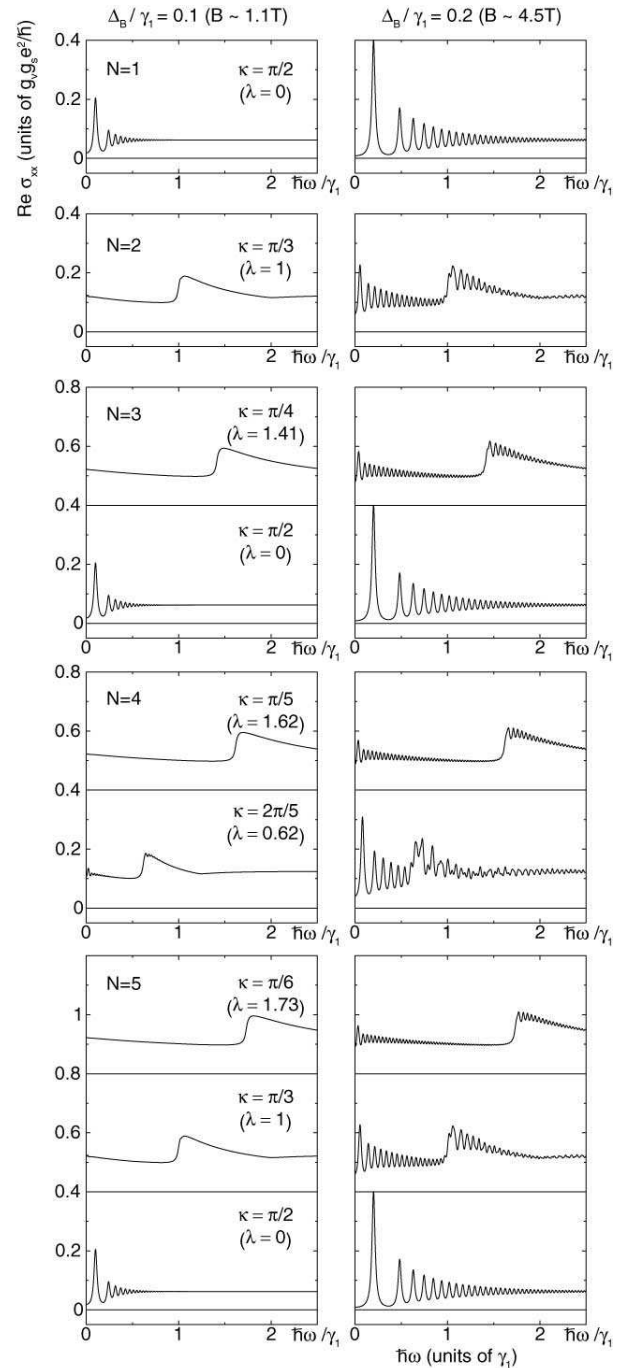


FIG. 3: Real part of the dynamical conductivity of $N = 1, 2, \dots, 5$ -layered graphenes as functions of the frequency, calculated for two different magnetic fields $\Delta_B/\gamma_1 = 0.1$ and 0.2 . We take $\Gamma/\gamma_1 = 0.01$.

In DOS, we observe the several peaks coming from the monolayer-type subband similarly to the optical absorption spectra. The peaks from the bilayer-type subband with $\kappa = 0$ become prominent in the high-field region $\Delta_B/\gamma_1 \gtrsim 0.2$. In LDOS, interestingly, the peaks of the monolayer-type subband are much more pronounced,

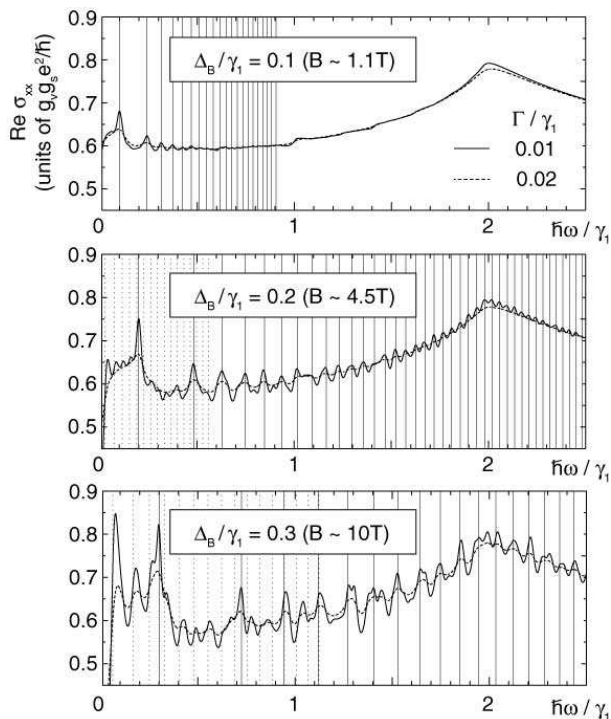


FIG. 4: Plots of $\text{Re } \sigma_{xx}(\omega)$ averaged over the layer numbers from $N = 1$ to 20, for magnetic fields with $\Delta_B/\gamma_1 = 0.1, 0.2$ and 0.3 . Vertical solid and dashed lines represent the ideal transition energies for the monolayer-type ($\kappa = \pi/2$) and the bilayer-type ($\kappa = 0$) subbands, respectively.

while those of $\kappa = 0$ are strongly suppressed. This can be understood by the wave function defined by Eq. (8). If we look at a state in the subband m in N -layered graphene, the wave amplitude on the top layer ($j = 1$) always acquires the factor $\psi_m(1) = \sqrt{2/(N+1)} \sin \kappa_m$. Obviously this takes maximum in the monolayer-type ($\kappa = \pi/2$) and zero at $\kappa = 0$, and thus the monolayer-type state contributes the most to the surface LDOS. The bilayer-type signals of the subbands $\kappa = \pi/3$ and $\pi/4$ are also visible in LDOS while they are hidden by $\kappa = 0$ in DOS.

IV. DISCUSSION

Recently the optical absorption spectrum was measured in the epitaxial thin graphite films and the monolayer-like signal was observed, while the detail profile of the system remains unclear. Similar \sqrt{B} -dependent features were also observed in the samples containing high-number of graphene layers (~ 100) grown on SiC substrate,⁴ and in a thin graphite sample of thickness ~ 100 nm exfoliated from highly-oriented pyrolytic graphite.⁵ Those results are nontrivial because, if the system is a real three-dimensional bulk graphite, the spectrum would be contributed mainly from the states around $k_z = 0$ ($\kappa = 0$ in our discussion) where the Landau levels

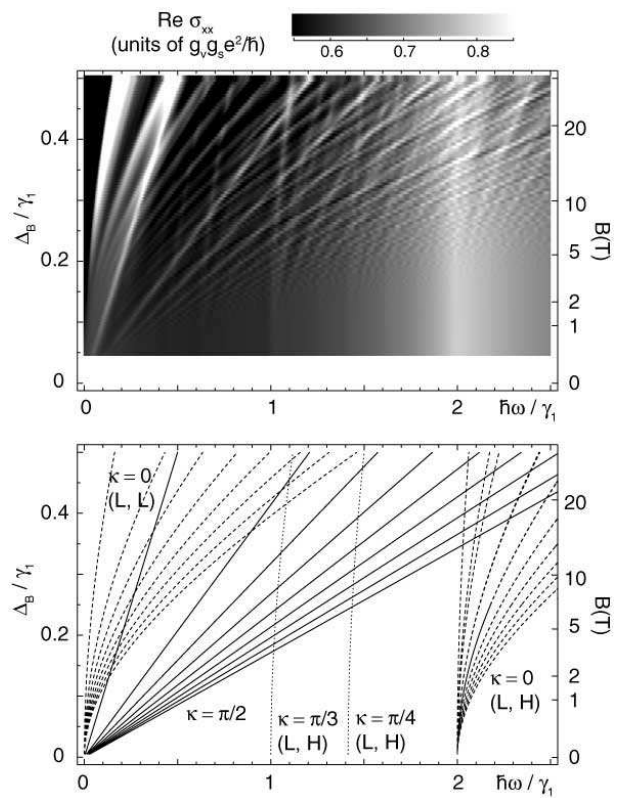


FIG. 5: (Top) Density plot of $\text{Re } \sigma_{xx}(\omega, \Delta_B)$ averaged over the layer numbers from $N = 1$ to 20. Γ is set to $0.01\gamma_1$. (Bottom) Corresponding plot for the transition energies between the several Landau levels.

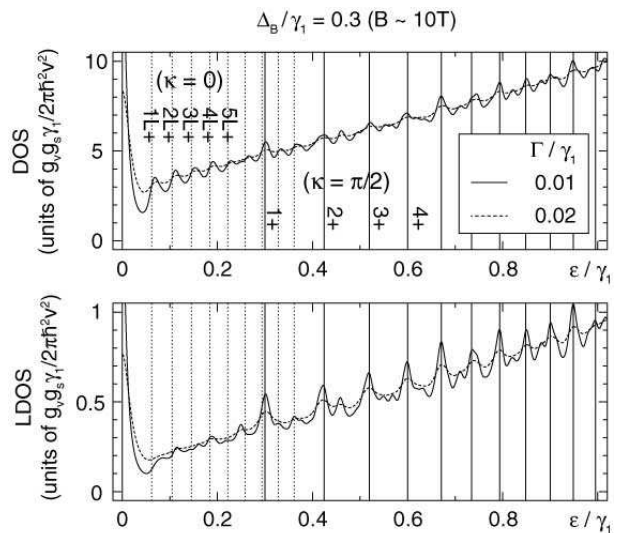


FIG. 6: (Top) Density of states averaged over the layer numbers $N = 1$ to 20, at $\Delta_B/\gamma_1 = 0.3$. (Bottom) Corresponding plot for the local density of states on the top layer. Vertical solid and dashed lines indicate the ideal Landau level energies for the monolayer-type ($\kappa = \pi/2$) and the bilayer-type ($\kappa = 0$) subbands, respectively.

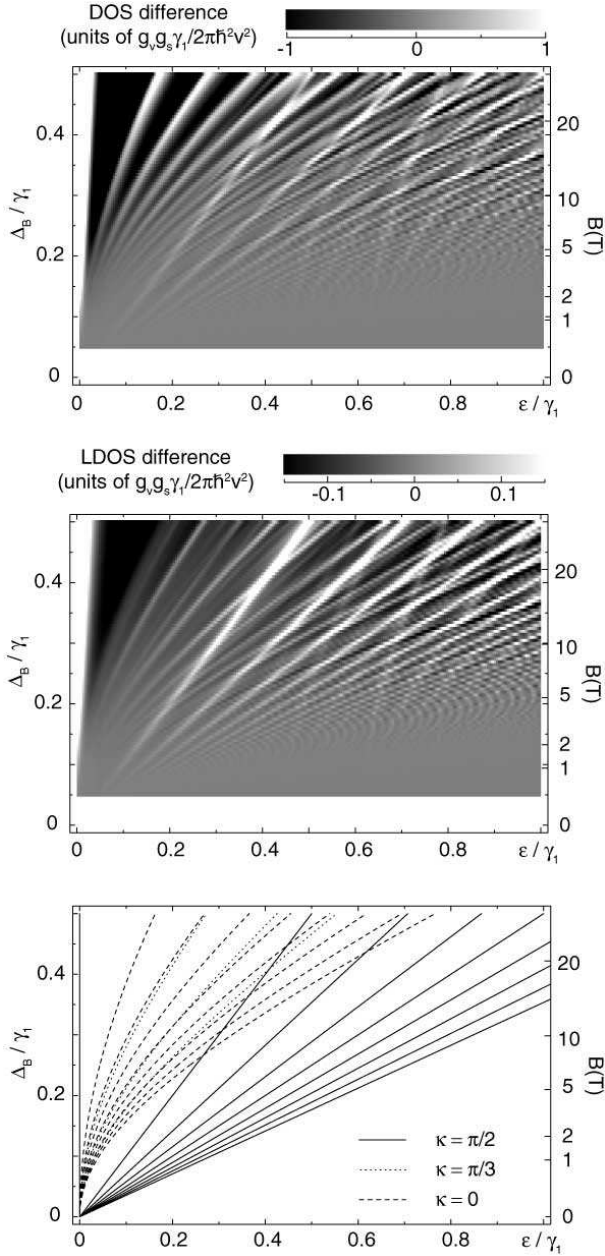


FIG. 7: (Top) Density of states (measured from the zero-field value) averaged over the layer numbers from $N = 1$ to 20, plotted in (ϵ, Δ_B) -plane. Γ is set to $0.01\gamma_1$. (Middle) Similar plot for the local density of states on the top layer. (Bottom) Ideal Landau level energies corresponding to several dominant peaks in above two panels.

are flat with respect to k_z . One possible scenario for this is that the system can be regarded as a compound of multilayer fragments with various small layer numbers, and the monolayer-like spectra of all the odd layers are observed. It should also be mentioned that the local density of states on the surface of graphite was observed in the experiment.^{47,48} Our calculation predicts that the pronounced monolayer-type spectrum would be observable

in a multilayer graphene.

While we adopted a simplified effective-mass model in which only γ_0 and γ_1 are included, here we briefly mention the effects of other hopping parameters. The parameter γ_3 neglected here couples group II atoms on neighboring layers. This is responsible for the trigonal warping of the band dispersion, but gives only a slight shift in the Landau level energies except for the low energy region (< 10 meV).^{33,34,35} Therefore, it would hardly affect the peak positions in the absorption spectra while may modify the amplitudes through the matrix element changes. The parameter γ_4 couples group I and II atoms sitting on the neighboring layers, such as $A_j \leftrightarrow A_{j+1}$ or $B_j \leftrightarrow B_{j+1}$. This parameter introduces a small electron-hole asymmetry in the band structure, but does not change the qualitative feature of the low-energy spectrum.⁴¹

We also neglected the vertical hopping between the second-nearest neighboring layers for group II and I atoms, which are parameterized by γ_2 and γ_5 , respectively. Including those parameters mainly shifts the zero energy (the band touching point) upward or downward, depending on each subsystem.^{25,26,27} in the tight-binding model^{26,27} and the density functional theory²⁵ estimate the shift δE at the order of 10 meV. In 3D limit, this corresponds to the band dispersion along k_z -direction.^{7,31,32,33,34,35} The zero-energy shift leads to the electron or hole doping, and gives a change of the absorption spectrum in the region $\hbar\omega \lesssim 2\delta E$.

The effective mass model is no longer valid when the energy is as high as the intra-layer coupling $\gamma_0 \sim 3$ eV. The lattice effect appears as trigonal warping in the band dispersion in higher energies,^{49,50,51} while this should be distinguished from the trigonal warping discussed above, which is due to the extra band parameter within the effective mass model. The frequency region covered in our calculation, $\hbar\omega \lesssim 2.5\gamma_1 \sim 1$ eV, roughly corresponds to the energy region $|\epsilon| \lesssim 0.5$ eV. The deviation in eigen energy is estimated at 5% at $\epsilon = 0.5$ eV and can be treated perturbationally,⁴⁹ although it grows as the energy increases out of this region. This anisotropy constitutes a major part of the chirality dependence of optical spectra in carbon nanotubes, enabling the assignment of the structure of individual nanotubes.⁵²

Lastly, while our model is based on the bulk 3D graphite, it should be noted that the band parameters in few-layered graphenes are not exactly the same as those for the bulk graphite, but generally vary depending on the layer number.¹⁹ There is a theoretical attempt to obtain accurate electronic structures for few-layered graphenes, using the density functional theory with the local density approximation.²⁵ The calculation beyond the local density approximation was also proposed, which properly treats nonlocal van der Waals interaction coupling graphene layers in the density functional framework.⁵³ The study of the optical absorption in a refined band model is left for a future work.

In conclusion, we have presented a systematic study

of the optical absorption properties and the density of states in the multilayer graphenes as a function of layer numbers. The spectrum can be understood through the decomposition into sub-components, each of which is equivalent to the monolayer graphene or the bilayer graphene with single parameter κ . We proposed that the monolayer-like spectra is possibly observed in the mixture of the multi-layered graphene, contributed by the effective monolayer subbands existing in every odd-layered graphene.

ACKNOWLEDGMENTS

The authors acknowledge helpful interactions with E. A. Henriksen, Z. Jiang, K. F. Mak, P. Kim, and T. F.

Heinz. This work has been supported in part by the 21st Century COE Program at Tokyo Tech “Nanometer-Scale Quantum Physics” and by Grants-in-Aid for Scientific Research and Priority Area “Carbon Nanotube Nano-Electronics” from the Ministry of Education, Culture, Sports, Science and Technology, Japan.

-
- ¹ M. L. Sadowski, G. Martinez, M. Potemski, C. Berger and W. A. de Heer, Phys. Rev. Lett. **97**, 266405 (2006)
- ² Z. Jiang, E. A. Henriksen, L. C. Tung, Y.-J. Wang, M. E. Schwartz, M.Y. Han, P. Kim, and H. L. Stormer, Phys. Rev. Lett. **98**, 197403 (2007).
- ³ R.S. Deacon, K.-C. Chuang, R. J. Nicholas, K.S. Novoselov, and A.K. Geim, arXiv:0704.0410v2 (2007).
- ⁴ P. Plochocka, C. Faugeras, M. Orlita, M.L. Sadowski, G. Martinez, M. Potemski, M.O. Goerbig, J.-N. Fuchs, C. Berger, W.A. de Heer, Phys. Rev. Lett. **100**, 087401 (2008).
- ⁵ M. Orlita, C. Faugeras, G. Martinez, D. K. Maude, M. L. Sadowski, and M. Potemski, Phys. Rev. Lett. (to be published).
- ⁶ E. A. Henriksen, Z. Jiang, L. C. Tung, M. E. Schwartz, M. Takita, Y.-J. Wang, P. Kim, and H. L. Stormer, Phys. Rev. Lett. **100**, 087403 (2008).
- ⁷ J. W. McClure, Phys. Rev. **104**, 666 (1956).
- ⁸ N. H. Shon and T. Ando, J. Phys. Soc. Jpn. **67**, 2421 (1998).
- ⁹ J. Gonzalez, F. Guinea, and M. A. H. Vozmediano, Phys. Rev. B **63**, 134421 (2001).
- ¹⁰ Y. Zheng and T. Ando, Phys. Rev. B **65**, 245420 (2002).
- ¹¹ T. Ando, Y. Zheng, and H. Suzuura, J. Phys. Soc. Jpn. **71**, 1318 (2002).
- ¹² H. Suzuura and T. Ando, Phys. Rev. Lett. **89**, 266603 (2002).
- ¹³ V. P. Gusynin and S. G. Sharapov, Phys. Rev. Lett. **95**, 146801 (2005).
- ¹⁴ K. S. Novoselov, A. K. Geim, S. V. Morozov, D. Jiang, Y. Zhang, S. V. Dubonos, I. V. Grigorieva, and A. A. Firsov, Science **306**, 666 (2004).
- ¹⁵ K. S. Novoselov, A. K. Geim, S. V. Morozov, D. Jiang, M. I. Katsnelson, I. V. Grigorieva, S. V. Dubonos, and A. A. Firsov, Nature **438**, 197 (2005).
- ¹⁶ Y. Zhang, Y. W. Tan, H. L. Stormer, and P. Kim, Nature **438**, 201 (2005).
- ¹⁷ V. P. Gusynin and S. G. Sharapov, Phys. Rev. B **73**, 245411 (2006).
- ¹⁸ V. P. Gusynin, S. G. Sharapov, and J. P. Carbotte, Phys. Rev. Lett. **96**, 256802 (2006); *ibid*, Phys. Rev. Lett. **98**, 157402 (2007)
- ¹⁹ T. Ohta, A. Bostwick, T. Seyller, K. Horn, and E. Rotenberg, Science **313**, 951 (2006); T. Ohta, A. Bostwick, J. L. McChesney, T. Seyller, K. Horn, and E. Rotenberg, Phys. Rev. Lett. **98**, 206802 (2007).
- ²⁰ Y. Kopelevich and P. Esquinazi, Advanced Materials **19**, 4559 (2007).
- ²¹ E. McCann and V. I. Fal’ko, Phys. Rev. Lett. **96**, 086805 (2006).
- ²² M. Koshino and T. Ando, Phys. Rev. B **73**, 245403 (2006).
- ²³ J. Nilsson, A. H. Castro Neto, F. Guinea, and N. M. R. Peres, Phys. Rev. Lett. **97**, 266801 (2006).
- ²⁴ F. Guinea, A. H. Castro Neto, and N. M. R. Peres, Phys. Rev. B **73**, 245426 (2006).
- ²⁵ S. Latil and L. Henrard, Phys. Rev. Lett. **97**, 036803 (2006).
- ²⁶ B. Partoens and F. M. Peeters, Phys. Rev. B **74**, 075404 (2006).
- ²⁷ C. L. Lu, C. P. Chang, Y. C. Huang, J. M. Lu, C. C. Hwang, and M. F. Lin, J. Phys. Condens. Matter **18**, 5849 (2006).
- ²⁸ M. Koshino and T. Ando, Phys. Rev. B **76**, 085425 (2007).
- ²⁹ W. W. Toy, M. S. Dresselhaus, and G. Dresselhaus, Phys. Rev. B **15**, 4077 (1977).
- ³⁰ S. Y. Zhou, G.-H. Gweon, J. Graf, A. V. Fedorov, C. D. Spataru, R. D. Diehl, Y. Kopelevich, D.-H. Lee, Steven G. Louie and A. Lanzara, Nat. Phys. **2**, 595 (2006)
- ³¹ J. W. McClure, Phys. Rev. **119**, 606 (1960).
- ³² M. Inoue, J. Phys. Soc. Jpn., **17**, 808 (1962).
- ³³ O. P. Gupta and P. R. Wallace, Phys. Status. solidi B **54**, 53 (1972).
- ³⁴ G. Dresselhaus, Phys. Rev. B **10**, 3602 (1974).
- ³⁵ K. Nakao, J. Phys. Soc. Jpn., **40**, 761 (1976).
- ³⁶ D. S. L. Abergel and V. I. Fal’ko Phys. Rev. B **75**, 155430 (2007).
- ³⁷ J. Milton Pereira Jr., F. M. Peeters, and P. Vasilopoulos, Phys. Rev. B **76**, 115419 (2007).
- ³⁸ T. Ando, J. Phys. Soc. Jpn. **38**, 989 (1975).
- ³⁹ P. R. Wallace, Phys. Rev. **71**, 622 (1947)
- ⁴⁰ J. C. Slonczewski and P. R. Weiss, Phys. Rev. **109**, 272 (1958).
- ⁴¹ J. W. McClure, Phys. Rev. **108**, 612 (1957); *ibid*, **119**, 606 (1960).

- ⁴² D. P. DiVincenzo and E. J. Mele, Phys. Rev. B **29**, 1685 (1984).
- ⁴³ T. Ando, J. Phys. Soc. Jpn. **74**, 777 (2005).
- ⁴⁴ H. Ajiki and T. Ando, J. Phys. Soc. Jpn. **62**, 1255 (1993).
- ⁴⁵ A. Misu, E. Mendez, and M. S. Dresselhaus, J. Phys. Soc. Jpn. **47**, 199 (1979).
- ⁴⁶ T. Ando, J. Phys. Soc. Jpn. **76**, 104711 (2007).
- ⁴⁷ T. Matsui, H. Kambara, Y. Niimi, K. Tagami, M. Tsukada, and H. Fukuyama, Phys. Rev. Lett. **94**, 226403 (2005)
- ⁴⁸ Y. Niimi, H. Kambara, T. Matsui, D. Yoshioka, and Hiroshi Fukuyama, Phys. Rev. Lett. **97**, 236804 (2006).
- ⁴⁹ H. Ajiki and T. Ando, J. Phys. Soc. Jpn. **65**, 505 (1996).
- ⁵⁰ R. Saito, G. Dresselhaus, and M. S. Dresselhaus Phys. Rev. B **61**, 2981 (2000).
- ⁵¹ A. Grüneis, R. Saito, Ge. G. Samsonidze, T. Kimura, M. A. Pimenta, A. Jorio, A. G. Souza Filho, G. Dresselhaus, and M. S. Dresselhaus, Phys. Rev. B **67**, 165402 (2003).
- ⁵² S. M. Bachilo, M. S. Strano, C. Kittrell, R. H. Hauge, R. E. Smalley, and R. B. Weisman, Science **298**, 2361 (2002).
- ⁵³ H. Rydberg, M. Dion, N. Jacobson, E. Schroder, P. Hyldgaard, S. I. Simak, D. C. Langreth, and B. I. Lundqvist, Phys. Rev. Lett. **91**, 126402 (2003); H. Rydberg, B. I. Lundqvist, D.C. Langreth, and M. Dion, Phys. Rev. B **62**, 6997 (2000).